Effect of crystal field engineering and Fermi level optimization on thermoelectric properties of $Ge_{1.01}Te$: Experimental investigation and theoretical insight

Ashutosh Kumar [1,*,†] Preeti Bhumla [2,*] Duraisamy Sivaprahasam [3] Saswata Bhattacharya [2,‡] and Nita Dragoe [1,§]
[1] ICMMO (UMR CNRS 8182), Université Paris-Saclay, F-91405 Orsay, France
[2] Department of Physics, Indian Institute of Technology Delhi, New Delhi 110016, India
[3] CAEM, ARCI, IIT Madras Research Park, Taramani, Chennai 600 113, India

(Received 31 January 2023; accepted 4 April 2023; published 19 April 2023)

This study shows a method of enhancing the thermoelectric properties of GeTe-based materials through Ti and Bi codoping on cation sites along with self-doping of Ge via simultaneous optimization of electronic (via crystal field engineering and precise Fermi level optimization) and thermal (via point-defect scattering) transport properties. Pristine GeTe has high carrier concentration n due to intrinsic Ge vacancies, a low Seebeck coefficient α, and high thermal conductivity κ. The Ge vacancy optimization and crystal field engineering result in an enhanced α via excess Ge and Ti doping, which is further improved by band structure engineering through Bi doping. As a result of improved α and the optimized Fermi level (carrier concentration), an enhanced power factor $\alpha^2\sigma$ is obtained for Ti-Bi codoped $Ge_{1.01}Te$. These experimental results are also evidenced by theoretical calculations of band structure and thermoelectric parameters using density functional theory and BOLTZTRAP calculations. A significant reduction in the phonon thermal conductivity κ_{ph} from ~3.5 to ~1.06 W m^{-1} K^{-1} at 300 K for Ti-Bi codoping in GeTe is attributed to point-defect scattering due to mass and strain field fluctuations. This decrease in κ_{ph} is in line with the Debye-Callaway model. Also, the phonon dispersion calculations show a decreasing group velocity in Ti-Bi co-doped GeTe, supporting the obtained reduced κ_{ph}. The strategies used in the present study significantly increase the effective mass, optimize the carrier concentration, and decrease phonon thermal conductivity while achieving an impressive maximum zT value of 1.75 at 773 K and an average zT of 1.03 for $Ge_{0.91}Ti_{0.02}Bi_{0.08}Te$ over a temperature range of 300–773 K.

DOI: 10.1103/PhysRevMaterials.7.045402

I. INTRODUCTION

Thermoelectric (TE) materials are distinctly important for power generation and solid-state cooling owing to their capability of reversible conversion of heat into electricity without any moving parts and are emerging solutions for the thermal management and energy efficiency caused by the ubiquity of waste heat in modern technological times [1,2]. The efficacy of a TE device is assessed by a dimensionless quantity, the figure of merit zT, which depends on the following physical parameters: the Seebeck coefficient α, electrical conductivity σ, total thermal conductivity [$\kappa = \kappa_e + \kappa_{ph}$, with electronic ($\kappa_e$) and lattice ($\kappa_{ph}$) contributions], and temperature T, with $zT = \alpha^2\sigma T/(\kappa = \kappa_e + \kappa_{ph})$. It is seen that achieving a high zT in a TE material is daunting due to the intertwining relations between these TE parameters. Several innovative strategies have been deployed to decouple electron and phonon transport in materials to achieve an elevated zT, including band-structure engineering [3–7], nanostructuring [8], the composite approach [9–12], and the high-entropy concept [13,14]. In other words, concurrent improvement in electronic transport and prohibition of phonon propagation is the most important criterion for high-performance TE materials, as shown in PbTe [15], SnSe [16], skutterudites [17], and half-Heusler compounds [18].

Doped semiconductors are promising for TE properties due to their suitable electronic structure. GeTe-based materials are one example, showing their applicability in mid-temperature-range applications; however, the large p-type carrier concentration (~10^{21} cm^{-3}) at 300 K in GeTe, stemming from intrinsic Ge, results in small α and high κ_e, which ultimately results in inferior TE performance [19]. Also, the large energy separation ΔE between light and heavy valence bands limits the increase in α. Further, the room temperature κ_{ph} for pristine GeTe (~3 W m^{-1} K^{-1}) is significantly higher than the theoretical minimum value (0.44 W m^{-1} K^{-1}) estimated using Cahill's model [20].

Since the absolute value of α decreases but σ and κ_e increase with carrier concentration n, optimizing n is one of the most important steps, followed by engineering electronic and phonon band structures to achieve desired TE parameters. A reduction in κ_{ph} can be realized via hierarchical architecture engineering [21], defect engineering [22], the composite approach [23], and other multiscale scattering center approaches [24,25]. Several innovative strategies, including alloying and band structure modifications, have been adopted to reduce the high hole carrier concentration and improve α in GeTe [26–28]. Bi^{3+} and Sb^{3+} aliovalent doping at the Ge^{2+} site

*These authors contributed equally to this work.
†ashutosh.kumar@universite-paris-saclay.fr
‡saswata@physics.iitd.ac.in
§nita.dragoe@universite-paris-saclay.fr

 ©2023 American Physical Society

has been employed to reduce the carrier concentration and decrease κ_{ph} due to phonon scattering through solid-solution point defects [29]. Also, such aliovalent doping causes ΔE between light and heavy bands to converge and hence improves α. However, large aliovalent doping reduces σ significantly. On the other hand, transition metal doping (such as Ti, Zn, Mn, etc.) has been adopted in the literature to cause ΔE to converge to achieve enhanced α [30–32].

As mentioned earlier, the optimization of the Fermi level (carrier concentration) is of the utmost importance to achieve higher zT in a TE material [33]. For pristine GeTe, the extremely high n owing to intrinsic Ge vacancies pushes the Fermi level deep into the valence band. Shuai *et al.* utilized Ge vacancy manipulation to achieve high zT in the Ge-rich GeTe system [34]. Herein, we deploy multiple strategies to achieve a significant improvement in zT (1.75 at 773 K) via systematic doping of Ti and Bi in vacancy-engineered $Ge_{1.01}Te$, assisted by the confluence effect of crystal field engineering, valence band convergence, and point-defect scattering. Excess Ge manipulates n, enhancing α and reducing κ_e at 300 K. Ti doping further improves α via crystal field engineering by decreasing the c/a ratio. Ti-Bi codoping further improves the band convergence that increases α, and reduces κ_{ph} owing to point-defect scattering. Further, theoretical understanding of the crystal field and band structure engineering for electronic transport followed by the calculation of TE parameters using the Boltzmann transport equation are provided. Phonon dispersion calculations further support the phonon engineering-mediated reduced lattice thermal conductivity.

II. METHODS

A. Experimental details

$Ge_{1.01-x-y}Ti_xBi_yTe$ ($0 \leqslant x \leqslant 0.02,\ 0 \leqslant y \leqslant 0.08$) was synthesized by direct melting of high-purity Ge, Ti, Bi, and Te (>99.99%, Alfa Aesar) in the stoichiometric amount in evacuated quartz ampoules (10^{-6} mbar). The sealed ampoules were heated at 1173 K for 8 h with a heating rate of 80 K/h, followed by quenching in water. The quenched ingots were further ground using a mortar and pestle to obtain a homogeneous mixture. The spark plasma sintering (SPS) technique was used to compact the powders using a graphite dye 12 mm in diameter. The sintering was done at 823 K in an Ar atmosphere with heating and cooling rates of 100 and 50 K/min, respectively, with a hold time of 15 min under uniaxial pressure of 60 MPa. The pressure was released slowly during cooling to avoid any crack in the sample due to thermal expansion. The sintered pellets were cut to the proper dimensions for electrical and thermal transport measurements. The structural characterization was done using the x-ray diffraction technique using a Bruker instrument ($\lambda = 1.5406$ Å). The surface morphology and chemical composition were observed on the surface of the polished (using an automatic grinding/polishing machine) pellet employing a scanning electron microscope equipped with energy dispersive x-ray spectroscopy (EDS). The Seebeck coefficient α and electrical conductivity σ were measured using the four-probe configuration in the Ar atmosphere over the wide temperature range of 300–773 K. The total thermal conductivity κ was calculated using the following relation: $\kappa = D\rho C_p$. The thermal diffusivity D was measured using the Laser flash technique (NETZSCH Instrument) in Ar atmosphere, ρ is the density of the sample calculated using the sample mass and its geometric volume, and C_p is the specific heat capacity calculated using the Dulong-Petit law. The uncertainties in the measurement of α and σ were 7% and 5%, respectively; the estimated uncertainty in D is 5%. The carrier concentration n of the samples was measured with Hall measurements at 300 K and applied magnetic field changing gradually between −1.0 and 1.0 T using a homemade setup.

B. Computational details

The density functional theory (DFT) [35,36] calculations were carried out using the plane-wave-based pseudopotential approach, as implemented in the Vienna Ab initio Simulation Package (VASP) [37,38]. The structural optimization of all the modeled structures was performed using the generalized gradient approximation expressed by the Perdew-Burke-Ernzerhof [39] exchange-correlation (ϵ_{xc}) functional. The self-consistency loop was converged with a total energy threshold of 0.01 meV by conjugate gradient minimization. The structures were fully relaxed until the Heymann-Feynman forces on each atom were less than 10^{-5} eV/Å for both pure and doped configurations. The effects of doping were considered by substituting Ti and Bi atoms at the specific sites of Ge atoms in a $2 \times 2 \times 2$ supercell consisting of 48 atoms. All the structures were visualized through the Visualization for Electronic and Structural Analysis (VESTA) [40] software. Spin-orbit coupling interactions owing to heavy atoms were included when calculating the electronic band structures and density of states. A $6 \times 6 \times 2$ k mesh was used for Brillouin zone sampling. The electron wave function was expanded in a plane-wave basis set with an energy cutoff of 600 eV. Phonon calculations were obtained within the harmonic approximation and using a finite-displacement method [41]. The phonon dispersion plots and group velocities were calculated using the PHONOPY package [42,43]. A $2 \times 2 \times 2$ supercell was set for the cubic GeTe containing 64 atoms, whereas, for the rhombohedral phase, a $3 \times 3 \times 1$ supercell containing 54 atoms was built. In the Ti-Bi codoped rhombohedral system, we used a $2 \times 2 \times 2$ supercell consisting of 96 atoms. The BoltzTraP code [44], based on Boltzmann transport theory, was used to evaluate thermoelectric properties. The starting parameters for the calculations were the values obtained from the refinement.

III. RESULTS AND DISCUSSION

A. Structural analysis

The x-ray diffraction (XRD) pattern for $Ge_{1.01-x-y}Ti_xBi_yTe$ ($0 \leqslant x \leqslant 0.02,\ 0 \leqslant y \leqslant 0.08$) samples after SPS are shown in Fig. 1(a). The XRD pattern reveals a single-phase formation for all the samples with minor peaks corresponding to Ge [shown by an asterisk in Fig. 1(a)]. This is attributed to the stoichiometric Ge-rich content present in each sample. The XRD patterns are further analyzed with rhombohedral structure (space group $R3m$) using Rietveld

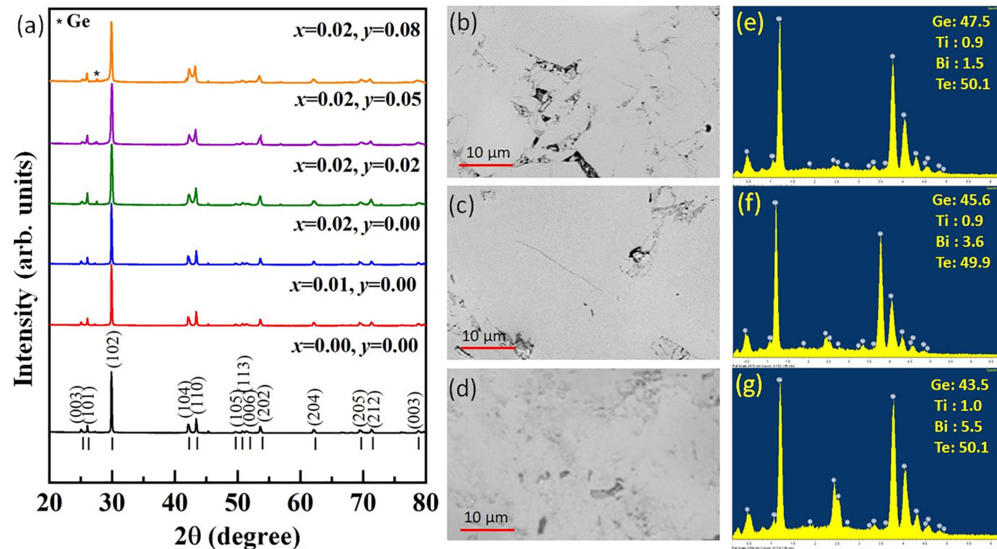

FIG. 1. (a) X-ray diffraction pattern of $Ge_{1.01-x-y}Ti_xBi_yTe$ ($0 \leqslant x \leqslant 0.02,\ 0 \leqslant y \leqslant 0.08$) at 300 K. The Bragg's position and corresponding Miller indices are marked for GeTe. Scanning electron microscopy images and corresponding energy dispersive x-ray spectra for $Ge_{1.01-x-y}Ti_xBi_yTe$ for (b) and (e) $x = 0.02$, $y = 0.02$, (c) and (f) $x = 0.02$, $y = 0.05$, and (d) and (g) $x = 0.02$, $y = 0.08$ are shown.

refinement employing FULLPROF software. The refinement pattern for $Ge_{0.91}Ti_{0.02}Bi_{0.08}Te$ is shown in Fig. S1 in the Supplemental Material (SM) [45]. The lattice parameters obtained from the Rietveld refinement of the XRD patterns for all the samples are shown in Table I. The lattice parameter for the c axis decreases from $c = 10.6762$ Å for $Ge_{1.01}Te$ to 10.6718 Å for $Ge_{0.99}Ti_{0.02}Te$, whereas the lattice parameter corresponding to the a axis increases from $a = 4.1624$ to 4.1627 Å. The overall c/a ratio and hence the volume of the unit cell decrease with Ti doping and are similar to Mn-doped GeTe [32]. Bi doping in $Ge_{0.99-y}Ti_{0.02}Bi_yTe$ further reduces the c/a ratio, as observed for only Ti-doped $Ge_{1.01}Te$ [30]. The lattice expansion may be attributed to the reduced Ge vacancies and the larger ionic radii of Ti^{2+} (0.86 Å) and Bi^{3+} (0.96 Å) in contrast to Ge^{2+} (0.73 Å) [46].

Surface morphology for $Ge_{1.01-x-y}Ti_xBi_yTe$ with different Ti-Bi codoping values is shown in Figs. 1(b)–1(d), and their corresponding energy dispersive x-ray spectra are shown in Figs. 1(e)–1(g). The homogeneous nature of the sample is seen on the surface. The EDS spectrum obtained from the surface is shown in Figs. 1(e)–1(g). The atomic percent values for the elements present in each sample are shown in the insets in Figs. 1(e)–1(g). The change in atomic percent of the elements is in line with the stoichiometric amount of Ti and Bi in $Ge_{1.01}Te$.

TABLE I. Lattice parameters a and c, c/a, carrier concentration n, and Seebeck coefficient α for $Ge_{1.01-x-y}Ti_xBi_yTe$ ($0.00 \leqslant x \leqslant 0.02$, $0.00 \leqslant y \leqslant 0.08$) at 300 K.

Sample x, y	a (Å)	c (Å)	c/a	n (10^{20} cm^{-3})	α (μV/K)
0.00, 0.00	4.1624	10.6762	2.5649	5.20	38
0.01, 0.00	4.1625	10.6745	2.5644	5.16	43
0.02, 0.00	4.1627	10.6718	2.5636	5.02	48
0.02, 0.02	4.1642	10.6502	2.5575	4.10	65
0.02, 0.05	4.1662	10.6212	2.5493	2.71	90
0.02, 0.08	4.1696	10.5816	2.5377	1.02	115

B. Electronic properties: Experiment

The temperature-dependent electrical conductivity σ for $Ge_{1.01-x-y}Ti_xBi_yTe$ ($0 \leqslant x \leqslant 0.02,\ 0 \leqslant y \leqslant 0.08$) is shown in Fig. 2(a). σ of $Ge_{1.01}Te$ is 6970 S cm^{-1}, smaller than that of pristine GeTe (∼7800 S cm^{-1}) at 300 K, and the difference is ascribed to the decrease in carrier concentration n in $Ge_{1.01}Te$ with diminishing Ge vacancies [33]. The formation energy of the Ge vacancy for the Ge-rich GeTe phase is larger than that of Te-rich GeTe [48]. This helps to suppress the Ge vacancy in the GeTe system, and hence, a lower carrier concentration is obtained. However, the electrical mobility μ improves with reduced n because (i) the interaction between the holes decreases with reduced n and (ii) the reduction in Ge vacancies also weakens the scattering of carriers [34]. It is worth noting that the dimension of holes is closer to the mean free path of the carriers, whereas Ge precipitates are micron sized. Hence, the Ge precipitates formed in Ge-rich samples do not influence μ like Ge vacancies due to their respective dimensions. In other words, the Ge-rich sample ($Ge_{1.01}Te$) reduces carrier concentration due to a reduction in intrinsic vacancies and enhances μ. σ for $Ge_{1.01}Te$ decreases with temperature, indicating a degenerate semiconductor behavior. A rapid change in σ across the temperature range of 600–700 K may be ascribed to the switching of the valence band between the L and Σ points mediated by the structural transition [49]. Further, Ti and Bi doping decreases σ across the temperature range studied and lowers the structural transition temperature as well. σ decrease from 6970 S cm^{-1} for $Ge_{1.01}Te$ to 3350 S cm^{-1} for $Ge_{0.99}Ti_{0.02}Te$ to 856 S cm^{-1} for $Ge_{0.91}Ti_{0.02}Sb_{0.08}Te$ at 300 K. It is noted that the Ti^{2+} doping does not reduce n significantly (see Table I). Further, the decrease in σ with Bi doping is ascribed to a strong reduction in n from 5.02×10^{20} cm^{-3} in $Ge_{0.99}Ti_{0.02}Te$ to

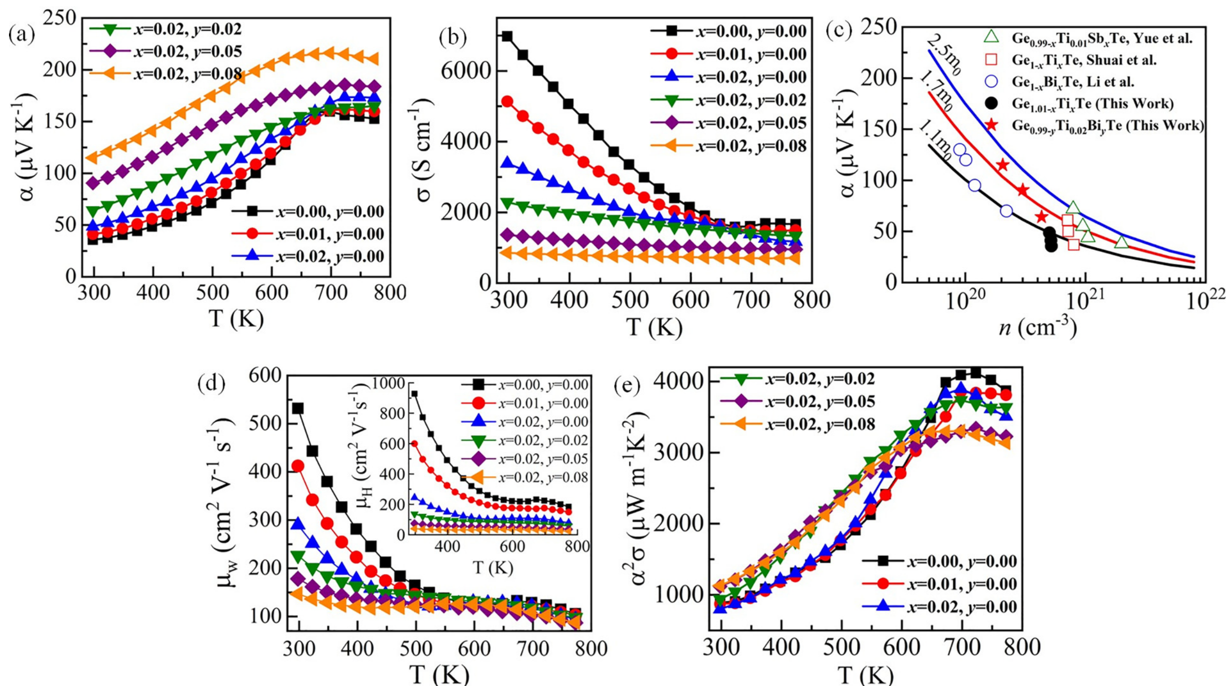

FIG. 2. Temperature-dependent (a) electrical conductivity σ and (b) Seebeck coefficient α for $Ge_{1.01-x-y}Ti_xBi_yTe$. (c) Room-temperature carrier concentration n dependence of α (Pisarenko plot), compared with literature: Yue *et al.* [30], Shuai *et al.* [34], and Li *et al.* [47]. (d) Temperature-dependent weighted mobility μ_w. Inset: Hall mobility μ_H. (e) Temperature-dependent power factor $\alpha^2\sigma$ for $Ge_{1.01-x-y}Ti_xBi_yTe$ $(0 \leqslant x \leqslant 0.02,\ 0 \leqslant y \leqslant 0.08)$.

$1.74 \times\ 10^{20}$ cm^{-3} in $Ge_{0.91}Ti_{0.02}Sb_{0.08}Te$ at 300 K. Bi^{3+} doping significantly reduces n by supplying extra valence electrons. Therefore, the carrier concentration is optimized with codoping of Ti and Bi, which matches the optimized carrier concentration.

The Seebeck coefficient α as a function of temperature $Ge_{1.01-x-y}Ti_xBi_yTe$ $(0 \leqslant x \leqslant 0.02,\ 0 \leqslant y \leqslant 0.08)$ is shown in Fig. 2(b). The positive sign of α indicates the p-type nature of transport and the dominating role of holes in electronic transport. It can be readily seen that α for $Ge_{1.01}Te$ is $\sim$38 μV K^{-1} at 300 K, higher than that of pristine GeTe ($\sim$27 μV K^{-1}). This rise in α is due to a reduction in n for Ge-rich samples. Further, α increases with Ti doping since Ti doping may induce resonant levels near the Fermi levels owing to the existence of partly filled spin-up channels. However, due to the high energy of d orbitals, the resonant level is induced close to the bottom of the conduction band and hence may not act to enlarge α. Further, it is noted that Ti doping does not reduce n, and the rise in α is attributed to the change in crystal field due to decreased c/a ratio in the sample [34]. Ti doping does improve α; however, n needs to be further reduced. Hence, Bi doping is further induced to optimize n and is beneficial for improving α and reducing κ_{ph} [50]. As can be seen in Table I, n decreases with Bi doping and results in an increase in α from 48 μV K^{-1} ($Ge_{0.99}Ti_{0.02}Te$) to 115 μV K^{-1}($Ge_{0.91}Ti_{0.02}Sb_{0.08}Te$) at 300 K. α increases with the rise in temperature for all the samples.

The change in α with Ti and Bi doping is further analyzed using a Pisarenko plot, as shown in Fig. 2(c). The α dependence on n is determined using the Kane model and two-band approximation (with different effective masses) and assuming acoustic phonons ($r = 0$) are the primary scattering mechanism [47]. α in the two-band approximation is expressed as

$$\alpha = -\frac{k_B}{e}\left[\frac{I^1_{r+1/2}(\eta^*, \beta)}{I^0_{r+1/2}(\eta^*, \beta)} - \eta^*\right], \tag{1}$$

where e is electronic charge, $\beta = k_BT/e_g$, e_g is the band gap, r is a scattering parameter, $\eta^* = (E_F - E_V)/k_BT$ is the reduced Fermi energy, and $I^k_{i,j}(\eta^*, \beta)$ are two parametric Fermi integrals, given as [51,52]

$$I^k_{i,j}(\eta^*, \beta) = \left(-\frac{df}{dx}\right)\frac{x^k(x+\beta x^2)^i dx}{(1+2\beta x)^j}. \tag{2}$$

Furthermore, the carrier concentration n, using the obtained values of η^*, is given as

$$n = \frac{(2m_{d,0}k_BT)^{3/2}}{2\pi^2h^3}I^0_{3/2,0}(\eta^*, \beta), \tag{3}$$

where $m_{d,0} = N_V^{2/3}(m_n^*)^{1/3}(m_\perp^*)^{2/3}$ is the band-edge density of states effective mass and N_V is band degeneracy.

n does not improve with Ti doping as in the case of Mn doping; however, the effective mass increases with an increase in the Ti content in the system [33]. Further, Ti-Bi codoping reduces n and gives rise to α. The effective mass increases in the Ti-Bi codoped samples. In the present case, the effective mass increases from 1.10 ($Ge_{0.99}Ti_{0.02}Te$) to 2.13 for $Ge_{0.91}Ti_{0.02}Bi_{0.08}Te$. This indicates that Bi doping enhances the effective mass because of the dominating conduction of

the heavy hole valence band over the light hole valence band. However, it is worth noting that the value of the effective mass depends on the choice of approximation used for the calculations (such as a single parabolic band and the Kane model) as well as band gap values, offset between the light and heavy hole bands, and hence, a comparison with the literature may not be precise. The increase in α for a Ti-Bi codoped sample is ascribed to the simultaneous optimization of n (through excess Ge content and Bi doping) and band engineering (band degeneration due to Bi and Ti codoping).

An understanding of charge carrier mobility is important for engineering semiconductor materials, which can be measured using the Hall effect. However, the weighted carrier mobility μ_w, which is defined as the carrier mobility weighted by the density of electronic states, can be estimated using the measured values of the Seebeck coefficient and electrical resistivity according to the following equation, as suggested by Snyder *et al.* [53]:

$$\mu_w = \frac{3h^3\sigma}{8\pi e(2m_e k_B T)^{3/2}} \times \left\{ \frac{\exp\left[\frac{|\alpha|}{k_B/e} - 2\right]}{1+\exp\left[-5\left(\frac{|\alpha|}{k_B/e} - 1\right)\right]} + \frac{\frac{3}{\pi^2}\frac{|\alpha|}{k_B/e}}{1+\exp\left[5\left(\frac{|\alpha|}{k_B/e} - 1\right)\right]} \right\}, \quad (4)$$

where k_B is the Boltzmann constant, m_e is the mass of an electron, h is Planck's constant, and e is the electronic charge. Also, μ_w is related to Hall mobility μ_H by the relation

$$\mu_w \approx \mu_H \left(\frac{m^*}{m_e}\right), \quad (5)$$

where m^* is the density of states electronic mass (effective mass). Since the density of electronic states is proportional to $m^{*3/2}$, μ_w is considered to be electron mobility weighted by the density of states. μ_w obtained for $Ge_{1.01-x-y}Ti_xBi_yTe$ ($0 \leqslant x \leqslant 0.02$, $0 \leqslant y \leqslant 0.08$) as a function of temperature is shown in Fig. 2(d). The inset shows the Hall mobility obtained from μ_w and the corresponding effective mass using Eq. (5). The change in μ_w for GeTe indicates a clear acoustic phonon-dominated transport; however, the samples with Ti-Bi codoping depict a weaker trend. Furthermore, the rise in μ_w at around 600–650 K may be ascribed to the rhombohedral-cubic structural phase transition, which leads to the convergence of the Σ and L bands and hence indicates a rise in the Seebeck coefficient. Also, the decrease in μ_w with temperature is indicative of enhanced scattering of carriers by phonons and holes.

The temperature-dependent α and σ are used to calculate the power factor $\alpha^2\sigma$ for the $Ge_{1.01-x-y}Ti_xBi_yTe$ ($0 \leqslant x \leqslant 0.02$, $0 \leqslant y \leqslant 0.08$) system, which is shown in Fig. 2(e). $\alpha^2\sigma$ increases with temperature for all the samples; however, it tends to decrease at higher temperatures, possibly due to the phase transition. The power factor for Ti-Bi codoped samples is larger at lower temperatures due to a significant increase in α.

C. Electronic properties: Theoretical insights

To gain insights into the experimental observations related to electronic transport in the Ti-Bi codoped GeTe system, DFT calculations were carried out to determine the electronic band structures and density of states for pristine, Ti-doped, and Ti-Bi codoped GeTe. We systematically doped Ge, Ti, and Ti-Bi in the GeTe system to obtain all the required configurations. The present calculations show that the principal valence band (light hole) maximum (VBM) and conduction band minimum (CBM) occur at the Γ point due to the folding of the L point onto Γ (see Fig. S2 in the SM) [45]. As pristine GeTe shows a high hole carrier concentration owing to the intrinsic Ge vacancies present in it, that has been considered in the DFT calculations. The electronic band structure for $Ge_{23}Te_{24}$ is shown in Fig. 3(a). (i) One Ti [Fig. 3(b)], (ii) one Ti and one Bi [Fig. 3(c)], and (iii) one Ti and two Bi atoms in place of Ge were substituted in the GeTe supercell. For the Ti-Bi codoped case, the energies of the two configurations were calculated, showing that (i) Ti and Bi atoms are close to each other and (ii) they are far from each other. The latter configuration has lower energy, making it more stable, and thus, the second configuration is considered for all further calculations (see Fig. S3 in the SM) [45]. As we can see in Fig. 3(b), the new impurity bands arise from the Ti states near the conduction band, which reduces the band gap. These resonant levels are induced below the conduction band owing to the high-energy Ti d orbitals and are consistent with previous studies [34]. The codoping of Ti and Bi at Ge in GeTe ($Ge_{21}TiBiTe_{24}$) further decreases the energy separation between the valence bands ΔE_Γ from 0.21 to 0.13 eV, which is further decreased to 0.08 eV in $Ge_{20}TiBi_2Te_{24}$, leading to band convergence in GeTe. This indicates that the heavy holes strongly influence carrier transport. Therefore, the Ti-Bi codoping in GeTe enhances the valence band convergence and confirms the obtained increase in the Seebeck coefficient.

Furthermore, we plotted the density of states (DOS) of $Ge_{25}Te_{24}$ (with excess Ge), followed by $Ge_{23}Te_{24}$ (with Ge vacancies), $Ge_{22}TiTe_{24}$ (Ti doped), and $Ge_{21}TiBiTe_{24}$ and $Ge_{20}TiBi_2Te_{24}$ (Ti-Bi codoped). The Fermi level position plays a vital role in optimizing the TE performance of any system. The high hole carrier concentration in GeTe deepens the Fermi level in the valence band. However, the DOS plot shows that the Fermi level lies in the middle of the band gap for pristine $Ge_{24}Te_{24}$ [33]. Therefore, we have theoretically introduced Ge vacancies in GeTe, due to which the Fermi level lies deep in the valence band and is in line with the experimental high carrier concentration present in GeTe. With excess Ge ($Ge_{25}Te_{24}$), the Fermi level tends to move towards the conduction band. The Ti doping in GeTe (with excess Ge) increases the carrier concentration, resulting in the shifting of E_F deeper in the valence band. Bi doping reduces the hole carrier concentration due to the donor nature of Bi. The decrease in the energy offset between the valence band edges results in band convergence in the codoped system, as shown in the band structure calculations. Therefore, the combination of both band convergence and the Fermi level position indicates an enlarged Seebeck coefficient in codoped samples. In addition, Ti-Bi codoping makes the DOS steeper, particularly near the valence band edge. This sharper DOS feature indicates a higher effective mass and enhances the Seebeck coefficient [54]. The Fermi level lies in the valence band for Ti and

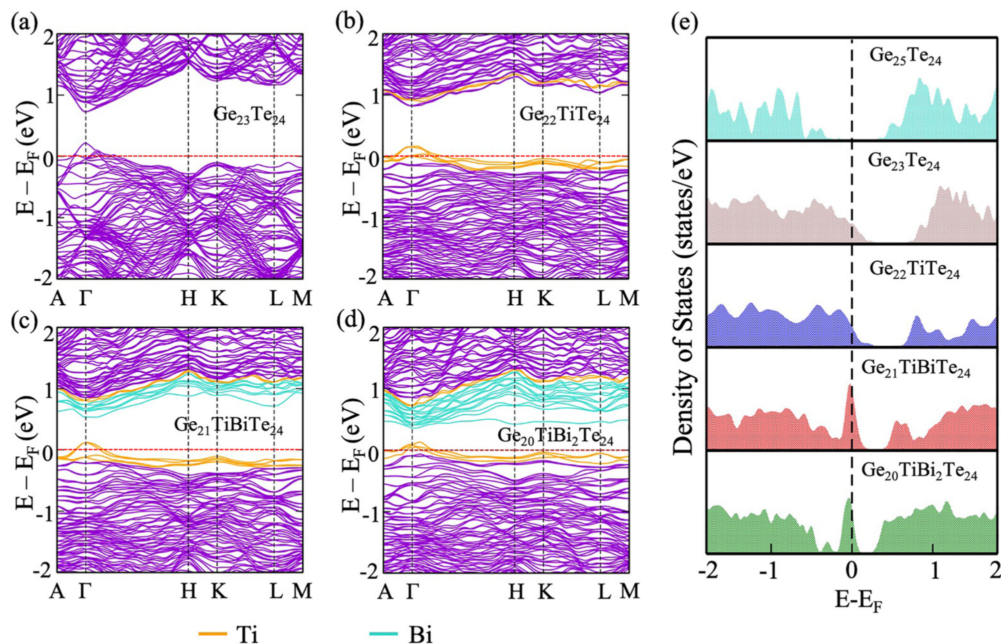

FIG. 3. Electronic band structures of (a) $Ge_{23}Te_{24}$, (b) $Ge_{22}TiTe_{24}$, (c) $Ge_{21}TiBiTe_{24}$, and (d) $Ge_{20}TiBi_2Te_{24}$. The Ge vacancies are theoretically induced during the calculation to attest to the large experimental value of the carrier concentration. The band gap appears at the Γ point in a 2 × 2 × 2 supercell containing 48 atoms. The VBM and CBM occur at the *L* point in the pristine GeTe fold on the Γ point in the supercell. (e) Density of states of GeTe with excess Ge ($Ge_{25}Te_{24}$), GeTe with Ge vacancies ($Ge_{23}Te_{24}$), Ti-doped GeTe ($Ge_{22}TiTe_{24}$), and Ti-Bi co-doped GeTe ($Ge_{21}TiBiTe_{24}$, $Ge_{20}TiBi_2Te_{24}$) samples.

Bi codoping because of the larger Ge vacancies considered during the theoretical calculations.

Subsequently, to examine the thermoelectric properties, we calculated the electrical conductivity σ, Seebeck coefficient α, thermal conductivity κ, power factor $\alpha^2\sigma$, and thermoelectric figure of merit zT for the $Ge_{23}Te_{24}$, $Ge_{22}TiTe_{24}$, $Ge_{21}TiBiTe_{24}$, and $Ge_{20}TiBi_2Te_{24}$ systems as a function of the chemical potential μ. Note that all μ-dependent transport properties are calculated by fixing the temperature and letting the carrier concentration n change. This implies that for a fixed temperature (here, 300 K), μ is a function of n. Studying thermoelectric properties with μ illustrates the doping of the carriers because it shows the addition (removal) of electrons to (from) the system. Advantageously, the position of μ determines the fraction of electrons in the conduction or valence band which take part in the electronic transport and hence influences the transport properties. Thus, we determine the thermoelectric parameters as a function of μ. Figure 4(b) shows the variation of the Seebeck coefficient with μ. α measures the induced thermoelectric voltage ΔV in response to a temperature difference ΔT in the material and is given as $\alpha = \Delta V/\Delta T$. By definition, $\mu = 0$ coincides with the top of the valence band in semiconductors. This implies that at $\mu = 0$, the nature of α determines the type of semiconductor. From Fig. 4(b), we can see that at $\mu = 0$, the value of α is positive for all GeTe systems, indicating that these are *p*-type semiconductors. α is also plotted as a function of temperature for the GeTe systems (see Fig. S4 in the SM) [45]. Since the calculation of κ_{ph} using state-of-the-art advanced methods (namely, the Green-Kubo method, nonequilibrium molecular dynamics, etc., especially for all doped configurations with broken symmetry) is computationally very expensive, we have opted to use the experimental value of κ_{ph} at 300 K to calculate zT according to the equation $zT = \alpha^2\sigma T/(\kappa = \kappa_e + \kappa_{ph})$. From Figs. 4(a) and 4(c), we see that electrical conductivity and thermal conductivity decrease with Ti-Bi doping, which is in line with the experimental findings. The increase in α with doping results in an increase in power factor values compared to the pristine system [see Fig. 4(d)]. The resonant peaks are observed near the Fermi level in the positive "μ" region. In addition, the zT values [Fig. 4(e)] are higher in the negative μ region than in the positive one, indicating that *p*-type doping has higher zT values. This hints that the considered codoped systems are promising *p*-type thermoelectric materials.

D. Thermal conductivity

The total thermal conductivity κ as a function of temperature for $Ge_{1.01-x-y}Ti_xBi_yTe$ ($0 \leqslant x \leqslant 0.02,\ 0 \leqslant y \leqslant 0.08$) is shown in Fig. 5(a). κ for Ti-doped and Ti-Bi codoped samples are lower than those of $Ge_{1.01}Te$ and GeTe systems. κ first decreases with Ti doping, and when Ti doping is kept constant at $x = 0.02$, κ decreases with further Bi doping. $Ge_{0.91}Ti_{0.02}Bi_{0.08}Te$ presents the lowest κ among all the samples studied across the whole temperature range. Also, κ decreases with the rise in temperature for all the samples, as is often observed in typical degenerate semiconductor solids. κ for pristine $Ge_{1.01}Te$ is 7.5 W m^{-1} K^{-1} at 300 K, decreases to 2.59 W m^{-1} K^{-1} at 673 K, and increases with a further rise in temperature due to the second-order structural transition, which is consistent with the change in σ with temperature [Fig. 2(a)]. Further, Ti doping lowers κ to 4.30 W m^{-1} K^{-1} at 300 K for $Ge_{0.99}Ti_{0.02}Te$, which is clearly due to reduced σ. Also, the codoping of Ti and Bi reduces κ to 1.53 W m^{-1} K^{-1} for $Ge_{0.91}Ti_{0.02}Bi_{0.08}Te$ at 300 K.

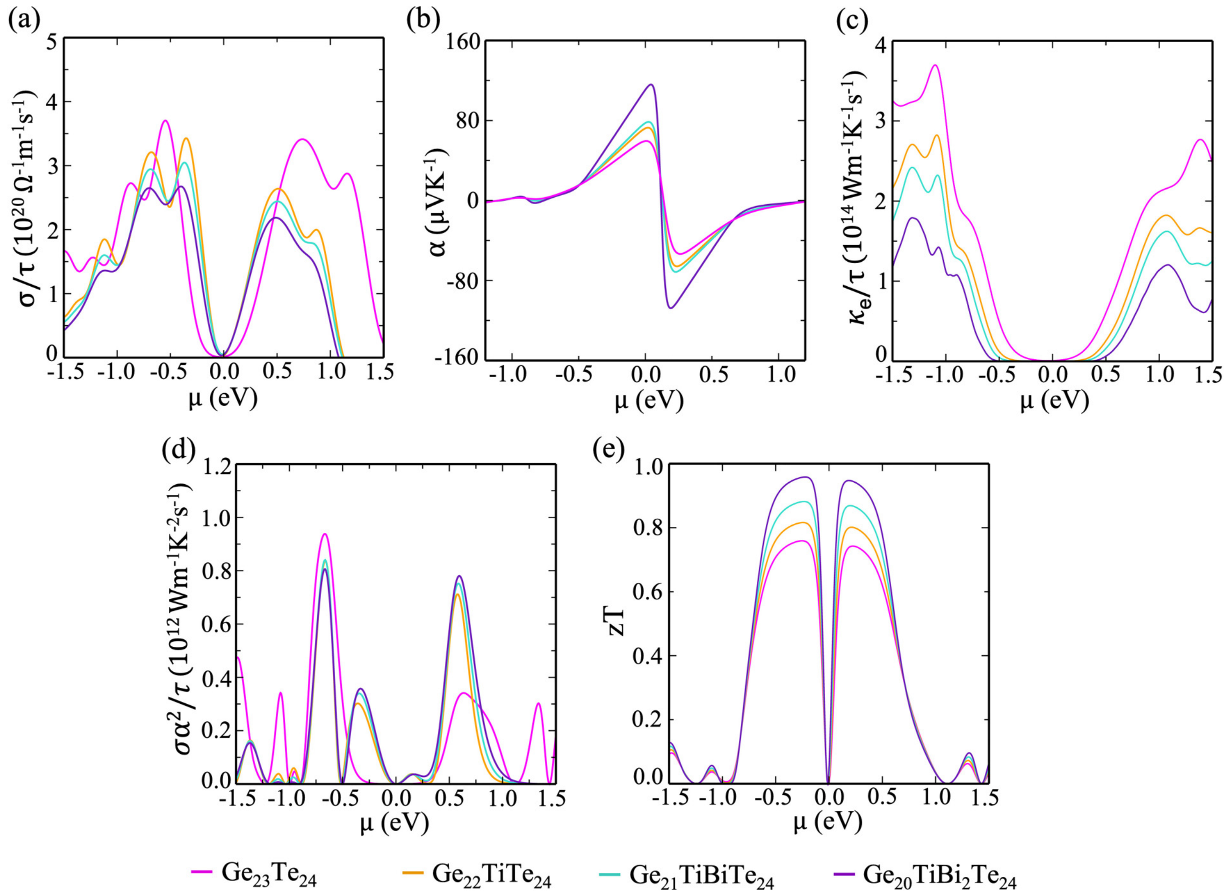

FIG. 4. (a) Electrical conductivity σ, (b) Seebeck coefficient α, (c) electronic thermal conductivity κ_e, (d) power factor $\alpha^2\sigma$, and (e) the figure of merit zT as a function of chemical potential μ calculated at 300 K for different GeTe compositions: $Ge_{23}Te_{24}$, $Ge_{22}TiTe_{24}$, $Ge_{21}TiBiTe_{24}$, and $Ge_{20}TiBi_2Te_{24}$. The electrical conductivity, electronic thermal conductivity, and power factor are reported by scaling them with τ.

Since κ consists of electronic thermal conductivity κ_e and phonon thermal conductivity κ_{ph}, it is important to understand the change in κ_e and κ_{ph} with Ti and Bi codoping in $Ge_{1.01}Te$. κ_e is calculated using the Wiedemann-Franz law: $\kappa_e = L\sigma T$, where the temperature-dependent Lorenz number L is obtained by estimating the reduced chemical potential from the temperature-dependent Seebeck coefficient considering the two-band model [33]. Temperature-dependent κ_e is shown in Fig. 5(b). The dramatic reduction in κ_e is correlated with reduced σ owing to reduced n in codoped samples. Further, κ_{ph} is extracted from κ by subtracting κ_e. The temperature-dependent κ_{ph} for $Ge_{1.01-x-y}Ti_xBi_yTe$ ($0 \leqslant x \leqslant 0.02$, $0 \leqslant y \leqslant 0.08$) is shown in Fig. 5(c). κ_{ph} for $Ge_{1.01}Te$ is 3.43 W m^{-1} K^{-1} at 300 K, and it reduces to 0.82 W m^{-1} K^{-1} at 673 K and then starts to increase above the transition temperature. It is possibly due to the ferroelectric instability close to the phase transition temperature as it induces soft optical phonon modes that strongly scatter the heat-carrying phonons [55]. Further, it is noted that κ_{ph} for $Ge_{1.01}Te$ is also influenced by the reduction in hole concentration. The decrease in hole concentration not only reduces σ but also reduces the phonon scattering due to a reduction in n, and hence, κ_{ph} is higher than that of GeTe ($\sim$3 W m^{-1} K^{-1} at 300 K). However, with Ti doping, κ_{ph} reduces to 2.30 W m^{-1} K^{-1}, and for the Ti-Bi codoped system, a reduced κ_{ph} of 1.05 W m^{-1} K^{-1} is obtained at 300 K, which further decreases to 0.57 W m^{-1} K^{-1} at 773 K for $Ge_{0.91}Ti_{0.02}Bi_{0.08}Te$. This suggests that Ti and Bi codoping significantly lowers κ_{ph} across the temperature range. Figure 5(d) shows κ_{ph} as a function of Ti and Bi codoping in $Ge_{1.01}Te$ at 300 K. The mass and strain field fluctuations in solid solutions result in point-defect scattering. κ_{ph} was calculated using the Debye-Callaway model, in which the ratio of phonon thermal conductivity with point defects κ_{ph} to the parent system κ_{ph}^p above the Debye temperature Θ_D is expressed as $\frac{\kappa_{\mathrm{ph}}}{\kappa_{\mathrm{ph}}^p} = \frac{\tan^{-1}(u)}{u}$, with $u = (\frac{\pi^2\Theta_D\Omega}{h\nu_a^2}\kappa_{\mathrm{ph}}^p\Gamma)^{1/2}$, where Ω, h, and ν_a are the average volume per atom, Planck's constant, and the average value of the sound velocity, respectively, and Γ is the scattering parameter consisting of mass and strain field fluctuations [33]. κ_{ph} obtained with the Debye-Callaway model is shown by the solid line in Fig. 5(d) and is in agreement with κ_{ph} obtained from κ. This decrease in κ_{ph} in the Ti-Bi codoped sample is hence attributed to point-defect scattering owing to mass and strain field fluctuations and agrees with the previous report of Mn-doped GeTe [33].

E. Phonon dispersion calculation

The underlying reason for the reduction in lattice thermal conductivity in Ti-Bi codoped GeTe can be understood

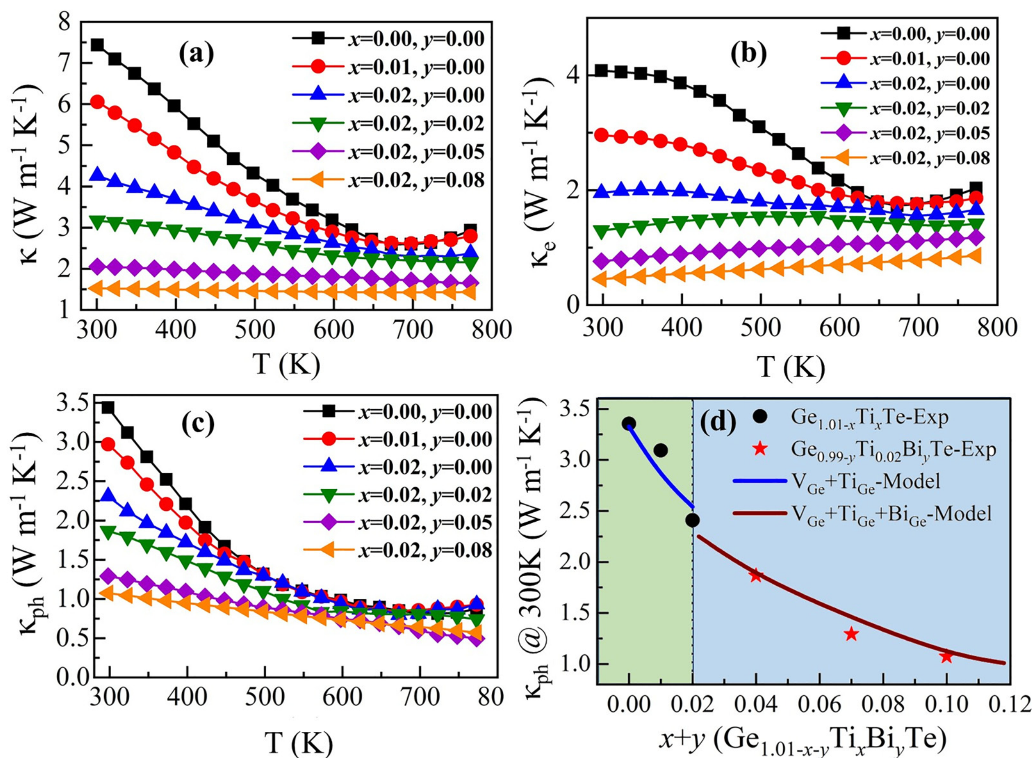

FIG. 5. (a) Total thermal conductivity κ, (b) electronic thermal conductivity κ_e, and (c) phonon thermal conductivity κ_{ph} as a function of temperature for $Ge_{1.01-x-y}Ti_xBi_yTe$ ($0 \leqslant x \leqslant 0.02,\ 0 \leqslant y \leqslant 0.08$). (d) Phonon thermal conductivity κ_{ph} as a function of Ti (x) and Bi (y) doping in $Ge_{1.01-x-y}Ti_xBi_yTe$ at 300 K. κ_{ph} calculated using the Debye-Callaway model is also shown.

by plotting the phonon dispersion curve. The phonon dispersion calculation for GeTe ($Ge_{24}Te_{24}$) and Ti-Bi codoped $Ge_{21}TiBi_2Te_{24}$ (vacancies are not considered while calculating the phonon dispersion plots due to the technical challenges in accommodating so many defects inside a supercell [33]) was performed to examine the dynamical stability. Figures 6(a) and 6(b) show the phonon dispersion plot for $Ge_{24}Te_{24}$ and $Ge_{21}TiBi_2Te_{24}$ in the rhombohedral structure. The phonon dispersion curve for GeTe is consistent with those of previous studies [56]. The phonon dispersion curve for Ti-Bi codoping shows a significant decrease in the phonon dispersion curve slope, as shown in Fig. 6(b). Generally, the phonon dispersion is shown by the ω vs k plot, and the gradient of the ω vs k curve measures v_g (phonon group velocity), where $v_g = d\omega/dk$. As shown in Fig. 6(b), the gradient of the phonon curve for the Ti-Bi codoped system is lower than that of GeTe at the Γ point [Fig. 6(a)]. This implies that the mean phonon group velocity decreases for the Ti-Bi codoped sample compared to GeTe, leading to a lower lattice thermal conductivity. The group velocities of both configurations throughout the Brillouin zone are given in Fig. S5 [45]. This decrease in the slope of the dispersion curve for Bi doping can be attributed to the large atomic mass M of Bi, as $\omega \propto M^{-1/2}$. Further, to examine the charge transfer, the charge density contours for $Ge_{24}Te_{24}$ and $Ge_{21}TiBi_2Te_{24}$ are computed (see Fig. S6 in the SM) [45]. As shown in Fig. S6, there is a charge transfer between the Bi and Ge atoms, which further stabilizes the bond. This stable bond hinders the free vibration of atoms and hence lowers the phonon group velocity.

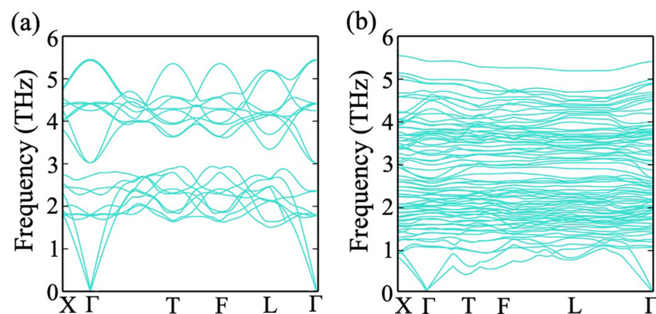

FIG. 6. Phonon dispersion curve for (a) $Ge_{24}Te_{24}$ and (b) $Ge_{21}TiBi_2Te_{24}$ in a rhombohedral structure.

F. Thermoelectric figure of merit

The TE figure of merit zT is calculated using the measured values of α, σ, and κ and is shown as a function of temperature for $Ge_{1.01-x-y}Ti_xBi_yTe$ ($0 \leqslant x \leqslant 0.02,\ 0 \leqslant y \leqslant 0.08$) in Fig. 7(a). zT increases with an increase in temperature for all the samples. A maximum zT of 1.09 is obtained for $Ge_{1.01}Te$ at 673 K, showing that vacancy engineering in GeTe itself improves its TE performance [57]. Further, zT increases to 1.21 at 723 K in Ti-doped samples, consistent with the results of previous studies [30]; however, a significant increase in zT is observed in the Ti-Bi codoped sample. It is attributed to the simultaneous optimization of band structure, carrier concentration, and phonon thermal conductivity. A maximum zT of 1.75 is obtained at 773 K for $Ge_{0.91}Ti_{0.02}Bi_{0.08}Te$. The

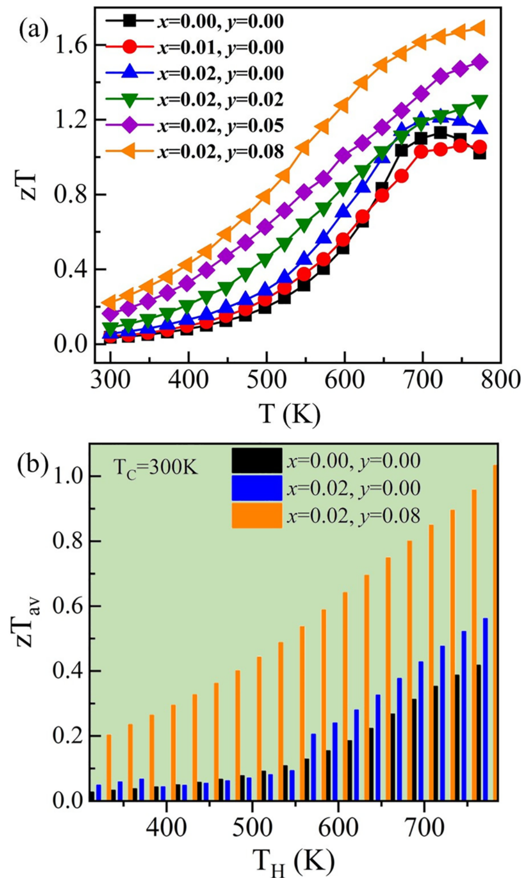

FIG. 7. (a) Figure of merit zT and (b) average figure of merit zT_{av} as a function of temperature for $Ge_{1.01-x-y}Ti_xBi_yTe$ ($0 \leqslant x \leqslant 0.02,\ 0 \leqslant y \leqslant 0.08$).

applicability of a TE material is quantified using its average zT ($zT_{\text{av}} = \int_{T_c}^{T_h} zT\,dT$). zT_{av} is calculated setting the lower (T_c) and upper (T_h) limits of temperature to 300 and 773 K, respectively, and is shown in Fig. 7(b). A maximum zT_{av} of 1.03 is obtained for $Ge_{0.91}Ti_{0.02}Bi_{0.08}Te$, which is significantly better than the recently reported values for several GeTe-based materials [32,58–61]. The theoretical energy conversion efficiency η is also calculated for $Ge_{0.91}Ti_{0.02}Bi_{0.08}Te$ (p-type leg) assuming a similar n-type leg for a temperature difference of 473 K. A maximum η of 14% is obtained in the present study, which is higher than the values for several TE materials reported in the literature [32,58–61].

IV. CONCLUSION

This study demonstrated the enhanced thermoelectric properties in Ti-Bi codoped $Ge_{1.01}Te$ accompanied by vacancy engineering. The samples synthesized using the melting-quenching-sintering process showed single-phase formation along with traces of Ge peaks due to the larger stoichiometric content, which was further supported by an electron microscopy analysis. The excess Ge reduces the carrier concentration n and hence adjusts the Fermi level position, which improves the TE performance of $Ge_{1.01}Te$. Further, Ti doping improves α due to crystal field engineering ascribed to a decreased c/a ratio, which is further enhanced by reducing n with Bi doping. The Ti-Bi codoped $Ge_{1.01}Te$ shows larger band degeneracy and hence improves α. The DFT calculations further verified the valence band convergence with Ti-Bi codoping and confirmed the obtained increase in α. A reduction in the total thermal conductivity κ due to decreased electrical conductivity and enhanced point-defect and mass fluctuation scatterings was obtained. The phonon dispersion calculations showed that phonon group velocity decreases in the Ti-Bi codoped system due to the larger atomic mass of Bi and the charge transfer between Bi and Ge atoms. With the combined effect of carrier concentration optimization, enhanced band degeneracy, and reduced phonon thermal conductivity κ_{ph}, a high zT of 1.75 at 773 K was obtained for $Ge_{0.91}Ti_{0.02}Bi_{0.08}Te$. This further results in an average zT of 1.03 for a temperature difference of 473 K, making it a promising candidate for practical applications. Also, a maximum energy conversion efficiency η of 14% was calculated assuming similar n-type materials, which are promising for thermoelectric devices.

ACKNOWLEDGMENTS

This work was supported by the French Agence Nationale de la Recherche (ANR), through the project NEO (Grant No. ANR 19-CE30-0030-01). P.B. acknowledges UGC, India, for the senior research fellowship [Grant No. 1392/(CSIR-UGC NET JUNE 2018)]. S.B. acknowledges financial support from SERB under a core research grant (Grant No. CRG/2019/000647) to set up his high-performance computing (HPC) facility "Veena" at IIT Delhi for computational resources.

[1] G. Tan, L. D. Zhao, and M. G. Kanatzidis, Rationally designing high-performance bulk thermoelectric materials, Chem. Rev. **116**, 12123 (2016).

[2] J. Mao, H. Zhu, Z. Ding, Z. Liu, G. A. Gamage, G. Chen, and Z. Ren, High thermoelectric cooling performance of N-type Mg_3Bi_2-based materials, Science **365**, 495 (2019).

[3] Y. Xiao, H. Wu, J. Cui, D. Wang, L. Fu, Y. Zhang, Y. Chen, J. He, S. J. Pennycook, and L. D. Zhao, Realizing high performance n-type PbTe by synergistically optimizing effective mass and carrier mobility and suppressing bipolar thermal conductivity, Energy Environ. Sci. **11**, 2486 (2018).

[4] L. Yang, Z. G. Chen, M. S. Dargusch, and J. Zou, High performance thermoelectric materials: Progress and their Applications, Adv. Energy Mater. **8**, 1701797 (2018).

[5] T. Mori, Novel principles and nanostructuring methods for enhanced thermoelectrics, Small **13**, 1702013 (2017).

[6] L. Xie, Y. Chen, R. Liu, E. Song, T. Xing, T. Deng, Q. Song, J. Liu, R. Zheng, X. Gao, S. Bai, and L. Chen, Stacking faults

modulation for scattering optimization in GeTe-based thermoelectric materials, Nano Energy **68**, 104347 (2020).

[7] Y. Yu, M. Cagnoni, O. Cojocaru-Mirédin, and M. Wuttig, Chalcogenide thermoelectrics empowered by an unconventional bonding mechanism, Adv. Funct. Mater. **30**, 1904862 (2020).

[8] D. Sivaprahasam, S. B. Chandrasekhar, S. Kashyap, A. Kumar, and R. Gopalan, Thermal conductivity of nanostructured $Fe_{0.04}Co_{0.96}Sb_3$ skutterudite, Mater. Lett. **252**, 231 (2019).

[9] A. Kumar, A. Kosonowski, P. Wyzga, and K. T. Wojciechowski, Effective thermal conductivity of $SrBi_4Ti_4O_{15}$-$La_{0.7}Sr_{0.3}MnO_3$ oxide composite: Role of particle size and interface thermal resistance, J. Eur. Ceram. Soc. **41**, 451 (2021).

[10] A. Kumar and K. T. Wojciechowski, Effect of interface resistance on thermoelectric properties in $(1-x)La_{0.95}Sr_{0.05}Co_{0.95}Mn_{0.05}O_3/(x)WC$ composite, J. Eur. Ceram. Soc. **42**, 4227 (2022).

[11] A. Kosonowski, A. Kumar, T. Parashchuk, R. Cardoso-Gil, and K. T. Wojciechowski, Thermal conductivity of PbTe–$CoSb_3$ bulk polycrystalline composite: Role of microstructure and interface thermal resistance, Dalton Trans. **50**, 1261 (2021).

[12] A. Kosonowski, A. Kumar, K. Wolski, S. Zapotoczny, and K. T. Wojciechowski, Origin of electrical contact resistance and its dominating effect on electrical conductivity in PbTe/$CoSb_3$ composite, J. Eur. Ceram. Soc. **42**, 2844 (2022).

[13] B. Jiang, Y. Yu, J. Cui, X. Liu, L. Xie, J. Liao, Q. Zhang, Y. Huang, S. Ning, B. Jia, B. Zhu, S. Bai, L. D. Chen, S. J. Pennycook, and J. He, High-entropy-stabilized chalcogenides with high thermoelectric performance, Science **371**, 830 (2021).

[14] A. Kumar, D. Dragoe, D. Berardan, and N. Dragoe, Thermoelectric properties of high-entropy rare-earth cobaltates, J. Materiomics **9**, 191 (2023).

[15] Y. Pei, A. LaLonde, S. Iwanaga, and G. J. Snyder, High thermoelectric figure of merit in heavy hole dominated PbTe, Energy Environ. Sci. **4**, 2085 (2011).

[16] L.-D. Zhao, S.-H. Lo, Y. Zhang, H. Sun, G. Tan, C. Uher, C. Wolverton, V. P. Dravid, and M. G. Kanatzidis, Ultralow thermal conductivity and high thermoelectric figure of merit in SnSe crystals, Nature (London) **508**, 373 (2014).

[17] Y. Tang, Z. M. Gibbs, L. A. Agapito, G. Li, H.-S. Kim, M. B. Nardelli, S. Curtarolo, and G. J. Snyder, Convergence of multi-valley bands as the electronic origin of high thermoelectric performance in $CoSb_3$ skutterudites, Nat. Mater. **14**, 1223 (2015).

[18] B. Hinterleitner, I. Knapp, M. Poneder, Y. Shi, H. Müller, G. Eguchi, C. Eisenmenger-Sittner, M. Stöger-Pollach, Y. Kakefuda, N. Kawamoto *et al.*, Thermoelectric performance of a metastable thin-film Heusler alloy, Nature (London) **576**, 85 (2019).

[19] S. Perumal, S. Roychowdhury, and K. Biswas, High performance thermoelectric materials and devices based on GeTe, J. Mater. Chem. C **4**, 7520 (2016).

[20] D. G. Cahill, and R. O. Pohl, Heat flow and lattice vibrations in glasses, Solid State Commun. **70**, 927 (1989).

[21] Y. Pei, G. Tan, D. Feng, L. Zheng, Q. Tan, X. Xie, S. Gong, Y. Chen, J. Li, J. He, M. G. Kanatzidis, and L. Zhao, Integrating band structure engineering with all-scale hierarchical structuring for high thermoelectric performance in PbTe system, Adv. Energy Mater. **7**, 1601450 (2017).

[22] J. Mao, Y. Wu, S. Song, Q. Zhu, J. Shuai, Z. Liu, Y. Pei, and Z. Ren, Defect engineering for realizing high thermoelectric performance in n-type Mg_3Sb_2–based materials, ACS Energy Lett. **2**, 2245 (2017).

[23] A. Kumar, P. Bhumla, A. Kosonowski, K. Wolski, S. Zapotoczny, S. Bhattacharya, and K. Wojciechowski, Synergistic effect of workfunction and acoustic impedance mismatch for improved thermoelectric performance in GeTe-WC composite, ACS Appl. Mater. Interfaces **14**, 44527 (2022).

[24] H. Liu, Z. Chen, J. Tang, Y. Zhong, X. Guo, F. Zhang, and R. Ang, High quality factor enabled by multiscale phonon scattering for enhancing thermoelectrics in low-solubility n-type PbTe–Cu_2Te alloys, ACS Appl. Mater. Interfaces **12**, 52952 (2020).

[25] T. Zhu, Y. Liu, C. Fu, J. P. Heremans, J. G. Snyder, and X. Zhao, Compromise and synergy in high-efficiency thermoelectric materials, Adv. Mater. **29**, 1605884 (2017).

[26] X. Zhang, J. Li, X. Wang, Z. Chen, J. Mao, Y. Chen, and Y. Pei, Vacancy manipulation for thermoelectric enhancements in GeTe alloys, J. Am. Chem. Soc. **140**, 15883 (2018).

[27] X. Zhang, Z. Bu, S. Lin, Z. Chen, W. Li, and Y. Pei, GeTe thermoelectrics, Joule **4**, 986 (2020).

[28] D. Wu, L.-D. Zhao, S. Hao, Q. Jiang, F. Zheng, J. W. Doak, H. Wu, H. Chi, Y. Gelbstein, C. Uher, C. Wolverton, M. Kanatzidis, and J. He, Origin of the high performance in GeTe-based thermoelectric materials upon Bi_2Te_3 doping, J. Am. Chem. Soc. **136**, 11412 (2014).

[29] S. Perumal, P. Bellare, U. S. Shenoy, U. V. Waghmare, and K. Biswas, Low thermal conductivity and high thermoelectric performance in Sb and Bi codoped GeTe: Complementary effect of band convergence and nanostructuring, Chem. Mater. **29**, 10426 (2017).

[30] L. Yue, W. Cui, S. Zheng, Y. Wu, L. Wang, P. Bai, and X. Dong, Band engineering and thermoelectric performance optimization of p-type GeTe-based alloys through Ti/Sb co-doping, J. Phys. Chem. C **124**, 5583 (2020).

[31] T. Mori, D. Berthebaud, T. Nishimura, A. Nomura, T. Shishido, and K. Nakajima, Effect of Zn doping on improving crystal quality and thermoelectric properties of borosilicides, Dalton Trans. **39**, 1027 (2010).

[32] J. K. Lee, M. W. Oh, B. S. Kim, B. K. Min, H. W. Lee, and S. D. Park, Influence of Mn on crystal structure and thermoelectric properties of GeTe compounds, Electron. Mater. Lett. **10**, 813 (2014).

[33] A. Kumar, P. Bhumla, T. Parashchuk, S. Baran, S. Bhattacharya, and K. T. Wojciechowski, Engineering electronic structure and lattice dynamics to achieve enhanced thermoelectric performance of Mn–Sb Co-doped GeTe, Chem. Mater. **33**, 3611 (2021).

[34] J. Shuai, Y. Sun, X. Tan, and T. Mori, Manipulating the Ge vacancies and Ge precipitates through Cr doping for realizing the high-performance GeTe thermoelectric material, Small **16**, 1906921 (2020).

[35] P. Hohenberg and W. Kohn, Inhomogeneous electron gas, Phys. Rev. **136**, B864 (1964).

[36] W. Kohn and L. J. Sham, Self-consistent equations including exchange and correlation effects, Phys. Rev. **140**, A1133 (1965).

[37] G. Kresse and J. Furthmuller, Efficiency of ab-initio total energy calculations for metals and semiconductors using a plane-wave basis set, Comput. Mater. Sci. **6**, 15 (1996).

[38] G. Kresse and D. Joubert, From ultrasoft pseudopotentials to the projector augmented-wave method, Phys. Rev. B **59**, 1758 (1999).

[39] J. P. Perdew, K. Burke, and M. Ernzerhof, Generalized Gradient Approximation Made Simple, Phys. Rev. Lett. **77**, 3865 (1996).

[40] K. Momma and F. Izumi, VESTA 3 for three-dimensional visualization of crystal, volumetric and morphology data, J. Appl. Crystallogr. **44**, 1272 (2011).

[41] K. Parlinski, Z. Li, and Y. Kawazoe, First-Principles Determination of the Soft Mode in Cubic ZrO_2, Phys. Rev. Lett. **78**, 4063 (1997).

[42] A. Togo and I. Tanaka, First principles phonon calculations in materials science, Scr. Mater. **108**, 1 (2015).

[43] A. Togo, F. Oba, and I. Tanaka, First-principles calculations of the ferroelastic transition between rutile-type and $CaCl_2$-type SiO_2 at high pressures, Phys. Rev. B **78**, 134106 (2008).

[44] G. Madsen and D. J. Singh, BoltzTraP: A code for calculating band-structure dependent quantities, Comput. Phys. Commun. **175**, 67 (2006).

[45] See Supplemental Material at http://link.aps.org/supplemental/10.1103/PhysRevMaterials.7.045402 for the Rietveld refinement pattern for $Ge_{0.91}Ti_{0.02}Bi_{0.08}Te$, the band structure for $Ge_{25}Te_{24}$, two structural configurations for $Ge_{20}TiBi_2Te_{24}$, the calculated Seebeck coefficient α as a function of temperature, group velocities for $Ge_{24}Te_{24}$ and $Ge_{21}TiBi_2Te_{24}$, and charge density plots for $Ge_{25}Te_{24}$ and $Ge_{20}TiBi_2Te_{24}$.

[46] R. D. Shannon, Revised effective ionic radii and systematic studies of interatomic distances in halides and chalcogenides, Acta Crystallogr., Sect. A **32**, 751 (1976).

[47] J. Li, X. Zhang, Z. Chen, S. Lin, W. Li, J. Shen, I. T. Witting, A. Faghaninia, Y. Chen, A. Jain, L. Chen, G. J. Snyder, and Y. Pei, Low-symmetry rhombohedral GeTe thermoelectrics, Joule **2**, 976 (2018).

[48] J. Dong, F.-H. Sun, H. Tang, J. Pei, H.-L. Zhuang, H.-H. Hu, B.-P. Zhang, Y. Pan, and J.-F. Li, Medium-temperature thermoelectric GeTe: Vacancy suppression and band structure engineering leading to high performance, Energy Environ. Sci. **12**, 1396 (2019).

[49] S. Perumal, M. Samanta, T. Ghosh, U. S. Shenoy, A. Bohra, S. Bhattacharya, A. Singh, U. V. Waghmare, and K. Biswas, Realization of high thermoelectric figure of merit in GeTe by complementary co-doping of Bi and In, Joule **3**, 2565 (2019).

[50] D. Wu, L. Xie, X. Xu, and J. He, High thermoelectric performance achieved in GeTe–Bi_2Te_3 pseudo-binary via van der Waals gap-induced hierarchical ferroelectric domain structure, Adv. Funct. Mater. **29**, 1806613 (2019).

[51] Y. I. Ravich, B. A. Efimova, and I. A. Smirnov, *Semiconducting Lead Chalcogenides* (Springer Science + Business Media, New York, 1970).

[52] N. K. Abrikosov, V. F. Bankina, L. V. Poretskaya, L. E. Shelimova, and E. V. Skudnova, *Semiconducting II–VI, IV–VI, and V–VI Compounds* (Springer Science + Business Media, New York, 1969).

[53] G. J. Snyder, A. H. Snyder, M. Wood, R. Gurunathan, B. H. Snyder, and C. Niu, Weighted mobility, Adv. Mater. **32**, 2001537 (2020).

[54] Z. Liu, J. Sun, J. Mao, H. Zhu, W. Ren, J. Zhou, Z. Wang, D. J. Singh, J. Sui, C. W. Chu, and Z. Ren, Phase-transition temperature suppression to achieve cubic GeTe and high thermoelectric performance by Bi and Mn codoping, Proc. Natl. Acad. Sci. USA **115**, 5332 (2018).

[55] S. Perumal, S. Roychowdhury, D. S. Negi, R. Datta, and K. Biswas, High thermoelectric performance and enhanced mechanical stability of p-type $Ge_{1-x}Sb_xTe$, Chem. Mater. **27**, 7171 (2015).

[56] U. D. Dowik, K. Parlinski, S. Rols, and T. Chatterji, Soft-phonon mediated structural phase transition in GeTe, Phys. Rev. B **89**, 224306 (2014).

[57] S. Roychowdhury, M. Samanta, S. Perumal, and K. Biswas, Germanium chalcogenide thermoelectrics: Electronic structure modulation and low lattice thermal conductivity, Chem. Mater. **30**, 5799 (2018).

[58] S. Perumal, S. Roychowdhury, and K. Biswas, Reduction of thermal conductivity through nanostructuring enhances the thermoelectric figure of merit in $Ge_{1-x}Bi_xTe$, Inorg. Chem. Front. **3**, 125 (2016).

[59] Z. Zheng, X. Su, R. Deng, C. Stoumpos, H. Xie, W. Liu, Y. Yan, S. Hao, C. Uher, C. Wolverton, M. G. Kanatzidis, and X. Tang, Rhombohedral to cubic conversion of GeTe via MnTe alloying leads to ultralow thermal conductivity, electronic band convergence, and high thermoelectric performance, J. Am. Chem. Soc. **140**, 2673 (2018).

[60] Z. W. Lu, J. Q. Li, C. Y. Wang, Y. Li, F. S. Liu, and W. Q. Ao, Effects of Mn substitution on the phases and thermoelectric properties of $Ge_{0.8}Pb_{0.2}Te$ alloy, J. Alloys Compd. **621**, 345 (2015).

[61] L. Wu, X. Li, S. Wang, T. Zhang, J. Yang, W. Zhang, L. Chen, and J. Yang, Resonant level-induced high thermoelectric response in indium-doped GeTe, NPG Asia Mater. **9**, e343 (2017).